CHEMISTRY OF MATERIALS
Cite This: Chem. Mater. 2018, 30, 8190−8200
Article
pubs.acs.org/cm

Li_3BO_3−Li_2CO_3: Rationally Designed Buffering Phase for Sulfide All-Solid-State Li-Ion Batteries

Sung Hoo Jung,[†,‡] Kyungbae Oh,[§] Young Jin Nam,[†,‡] Dae Yang Oh,[†,‡] Philipp Brüner,[∥] Kisuk Kang,*[,§] and Yoon Seok Jung*[,†]

[†]Department of Energy Engineering, Hanyang University, Seoul 04763, Republic of Korea
[‡]School of Energy and Chemical Engineering, Ulsan National Institute of Science and Technology (UNIST), Ulsan 44919, Republic of Korea
[§]Department of Materials Science and Engineering, Seoul National University, 1 Gwanak-ro, Gwanak-gu, Seoul 08826, Republic of Korea
[∥]IONTOF GmbH, Heisenbergstr. 15, 48149 Münster, Germany

Supporting Information

ABSTRACT: Most inorganic solid electrolytes (SEs) suffer from narrow intrinsic electrochemical windows and incompatibility with electrode materials, which results in the below par electrochemical performances of all-solid-state Li-ion or Li batteries (ASLBs). Unfortunately, in-depth understanding on the interfacial evolution and interfacial engineering via scalable protocols for ASLBs to mitigate these issues are at an infancy stage. Herein, we report on rationally designed Li_3BO_3−Li_2CO_3 (LBO-LCO or $Li_{3-x}B_{1-x}C_xO_3$ (LBCO)) coatings for $LiCoO_2$ in ASLBs employing sulfide SE of Li_6PS_5Cl. The new aqueous-solution-based LBO-coating protocol allows us to convert the surface impurity on $LiCoO_2$ and Li_2CO_3, into highly Li^+-conductive LBCO layers (6.0×10^{-7} S cm^{-1} at 30 °C for LBCO vs 1.4×10^{-9} S cm^{-1} at 100 °C for Li_2CO_3 or 1.4×10^{-9} S cm^{-1} at 30 °C for LBO), which also offer interfacial stability with sulfide SE. By applying these high-surface-coverage LBCO coatings, significantly enhanced electrochemical performances are obtained in terms of capacity, rate capability, and durability. It is elucidated that the LBCO coatings suppress the evolution of detrimental mixed conducting interphases containing Co_3S_4 and effectively passivate the interfaces by the formation of alternative interface phases.

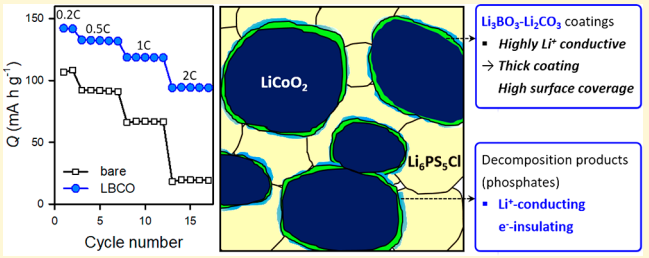

INTRODUCTION

Over the past decades, rechargeable lithium-ion batteries (LIBs) have conquered the market of energy storage devices owing to their superior energy density to their competitors. However, harsh efforts to maximize the energy density of LIBs, such as the use of ultrathin separators (≤10 μm) and raising the upper limit of voltages, have brought unprecedented risks in safety, which originates from the use of flammable organic liquid electrolytes.[1−8] Moreover, the safety concerns of LIBs are imperative for emerging large-scale applications, such as battery-driven electric vehicles and grid-scale energy storage.[9,10] In this regard, solidifying electrolytes with nonflammable inorganic materials is one of the best solutions.[10−18] Additionally, inorganic solid electrolytes (SEs) are considered enablers for next-generation electrode materials, such as Li metal and S (or Li_2S), which typically suffer from poor compatibility with conventional organic liquid electrolytes.[10,17−21]

Sulfide SE materials are some of the most promising candidates to realize high-performance all-solid-state batteries. Several state-of-the-art sulfide superionic conductors developed (e.g., $Li_{10}GeP_2S_{12}$,[22] $Li_{9.54}Si_{1.74}P_{1.44}S_{11.7}Cl_{0.3}$,[11] $Li_7P_3S_{11}$[23]) have shown impressively high ionic conductivities reaching the order of 10^{-2} S cm^{-1} at room temperature with a single ionic transport nature, which implies the feasibility of all-solid-state batteries significantly outperforming conventional LIBs.[24,25] More importantly, sulfide materials are mechanically sinterable at room temperature and are thus beneficial for practical electrode fabrication.[10,26,27]

Recent theoretical studies showed that, similar to organic liquid electrolytes for conventional LIBs, inorganic SE materials also have narrow intrinsic electrochemical windows, and that the passivation of SEs is necessary for the reversible operation of all-solid-state batteries.[28−32] In particular, the adaptation of conventional Li_xMO_2 (M = Co, Ni, Mn) cathode materials to all-solid-state Li-ion or Li batteries (ASLBs) suffers from huge interfacial resistances, which could be attributed to multiple factors such as surface impurities on Li_xMO_2,[33] severe reactions between Li_xMO_2 and sulfide SEs,[28,32,34] space charge layer effects,[35] lattice mismatches,[36]

Received: August 5, 2018
Revised: October 18, 2018
Published: October 19, 2018

DOI: 10.1021/acs.chemmater.8b03321
Chem. Mater. 2018, 30, 8190−8200

and poor wetting of SEs.[12,13,37] It is known that the formation of surface impurities, such as LiOH and Li_2CO_3 on Li_xMO_2 in ambient atmosphere conditions, causes the degradation of the electrochemical performances of conventional LIBs.[38−40] When it comes to ASLBs, the poor ion-conducting properties of the surface impurities could be more problematic.[33,41]

Since the first report in which it was demonstrated that interfacial engineering on $LiCoO_2$ using $Li_4Ti_5O_{12}$ could significantly lower the interfacial resistances in ASLBs,[35] various protective coatings have been developed (Table S1) to date: $LiNbO_3$,[11,12,42] Li_2SiO_3,[34] Ta_2O_5,[43] Al_2O_3,[44] and Li_3PO_4.[45] In most previous works regarding ASLBs using Li_xMO_2 and sulfide SEs, Li_xMO_2 coated with these materials was tested without placing a strong emphasis on the mechanistic details of the coatings.[10−12,16,22,25,26,37] Moreover, to date, only a few in-depth and/or systematic studies on Li_xMO_2/SE interfacial evolution/engineering have been reported.[32,34,45−47] The general consensus from the previous reports is that the interfacial resistance of ASLBs is inversely proportional to the Li^+ conductivity of the coating materials.[45] For example, using an amorphous $Li_{3.5}Si_{0.5}P_{0.5}O_4$ coating with a high Li^+ conductivity of 1.6×10^{-6} S cm^{-1} at room temperature resulted in a promising electrochemical performance of $LiCoO_2$/In ASLBs,[45] though the high ionic conductivity of the coating material could be achieved only for its amorphous form, derived by a costly vacuum deposition process. $LiNbO_3$ is one of the most frequently practiced coating materials for sulfide ASLBs because of its high Li^+ conductivity of $\sim 10^{-6}$ S cm^{-1} at room temperature and easy preparation protocol based on a wet method using alcohols (Table S1).[10−12,16,22,25,26,37,42] However, Nb is not earth-abundant and the use of flammable alcohol in the coating process would be a concern when scaling up. While these findings on the correlation between the Li^+ conductivity of the coating materials and the electrochemical performance aid in the design of alternative coating materials, it should be noted that the multiple aspects of not only Li^+ conductivity but also scalable preparation and cost-effectiveness should be carefully considered. Moreover, a detailed understanding on the evolution at electrode−SE interfaces affected by protective coatings is required. These aspects are imperative for the practical development of high-performance ASLBs.

From this background, Li_3BO_3 (LBO) has caught our attention. Despite its relatively low Li^+ conductivity (1.4×10^{-9} S cm^{-1} at 30 °C, measured in this work), LBO has been investigated as a sintering aid for oxide SE materials, such as $Li_7La_3Zr_2O_{12}$, for oxide-based ASLBs, as it can help lower the sintering temperatures for the oxide SEs because of its low melting point (700 °C).[48−53] However, until now, there has been no report on the application of LBO or LBO-derived materials for sulfide-based ASLBs. Herein, we report the development of rationally designed Li_3BO_3−Li_2CO_3 (LBO-LCO or $Li_{3-x}B_{1-x}C_xO_3$ (LBCO)) protective coatings prepared via a simple and scalable wet protocol using water, which drastically enhances the electrochemical performances of $LiCoO_2$ for ASLBs using sulfide SEs. The surface impurity on $LiCoO_2$, Li_2CO_3, generally impedes Li^+ transport at the interfaces, but after the aforementioned wet-coating process for LBO, it is converted into highly Li^+ conductive LBCO coating layers. Complementary analyses reveal that the as-derived highly conductive, thick, and high-surface-coverage LBCO coatings for $LiCoO_2$ effectively suppress the formation of detrimental Co_3S_4 phase and form good passivating layers comprised of phosphates, thus minimizing interfacial resistances. This is also supported by our thermodynamic computational results based on first-principles calculations regarding various states of mixed phases. Compared with other coating materials, LBCO and its precursor are cost-effective and environmentally benign (Table S1). Moreover, the use of water as a solvent is a significant advantage which avoids the use of flammable solvents employed in typical coating procedures.

RESULTS AND DISCUSSION

In our screening process for potential coating materials, we first carried out computational investigations to examine the phase stability at applied Li potential which corresponds to the intrinsic electrochemical window in Li electrochemical system.[28,30,31] The relatively stable nature of LBO and LBCO at high Li potential compared with Li_6PS_5Cl (LPSCl) suggests the potential use of LBO and LBCO as coating

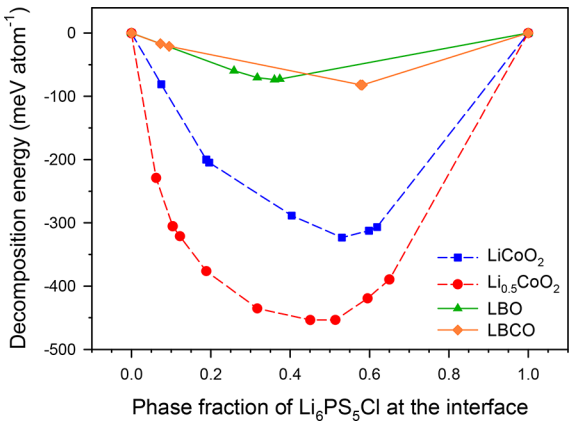

Figure 1. Calculated mutual decomposition energy of Li_6PS_5Cl with pristine and delithiated $LiCoO_2$, LBO (Li_3BO_3), and LBCO ($Li_{3-x}B_{1-x}C_xO_3$, $x = 0.80$) at various phase fractions of Li_6PS_5Cl in the mixed compounds.

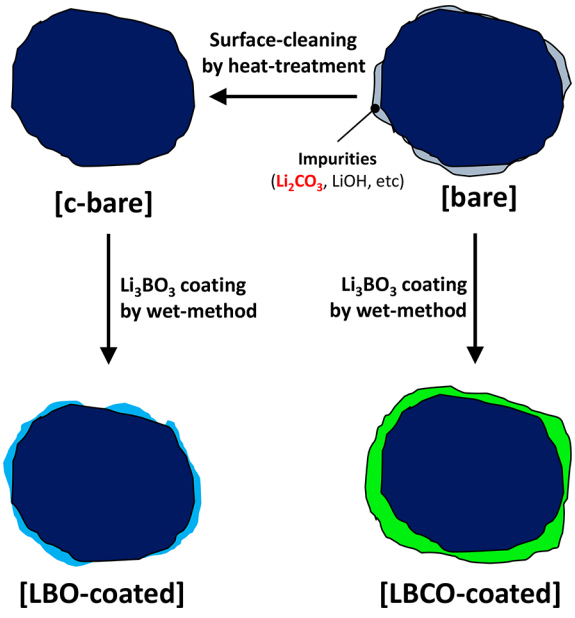

Figure 2. Schematic diagram illustrating bare, c-bare, LBO-coated, and LBCO-coated $LiCoO_2$.

DOI: 10.1021/acs.chemmater.8b03321
Chem. Mater. 2018, 30, 8190−8200

Table 1. Characteristics of LBO(-LCO) Coatings for $LiCoO_2$

	wt % of the coatings				
sample	Li_3BO_3[a]	$Li_{3-x}B_{1-x}C_xO_3$[b]	x in $Li_{3-x}B_{1-x}C_xO_3$[a]	thickness of the coating (nm)[d]	relative surface coverage (%)[e]
bare	0	-	-	-	21
c-bare	0	-	-	-	0
LBO	0.05 (0.06)[b]	-	0.00	1.0	-
	0.1 (0.15)[b]	-	0.00	2.5	-
	0.5 (0.63)[b]	-	0.00	10.4	79
LBCO	0.1	1.24	0.10	21.5	-
	0.5	1.72 (1.62)[c]	0.35 (0.33)[c]	29.4	87
	1.0	2.18 (2.08)[c]	0.50 (0.48)[c]	37.0	-
a-LBCO	0.5	1.72	0.35	29.4	88

[a]Targeting values. [b]Obtained by ICP-OES and TGA measurements. [c]Obtained by ICP-OES and elemental analyzer measurements. [d]Calculated based on the surface area of $LiCoO_2$, obtained by N_2 adsorption−desorption isotherm measurements (0.29 m^2 g^{-1}). [e]Obtained by LEIS measurements. Surface coverage for c-bare $LiCoO_2$ is assumed to be 0%.

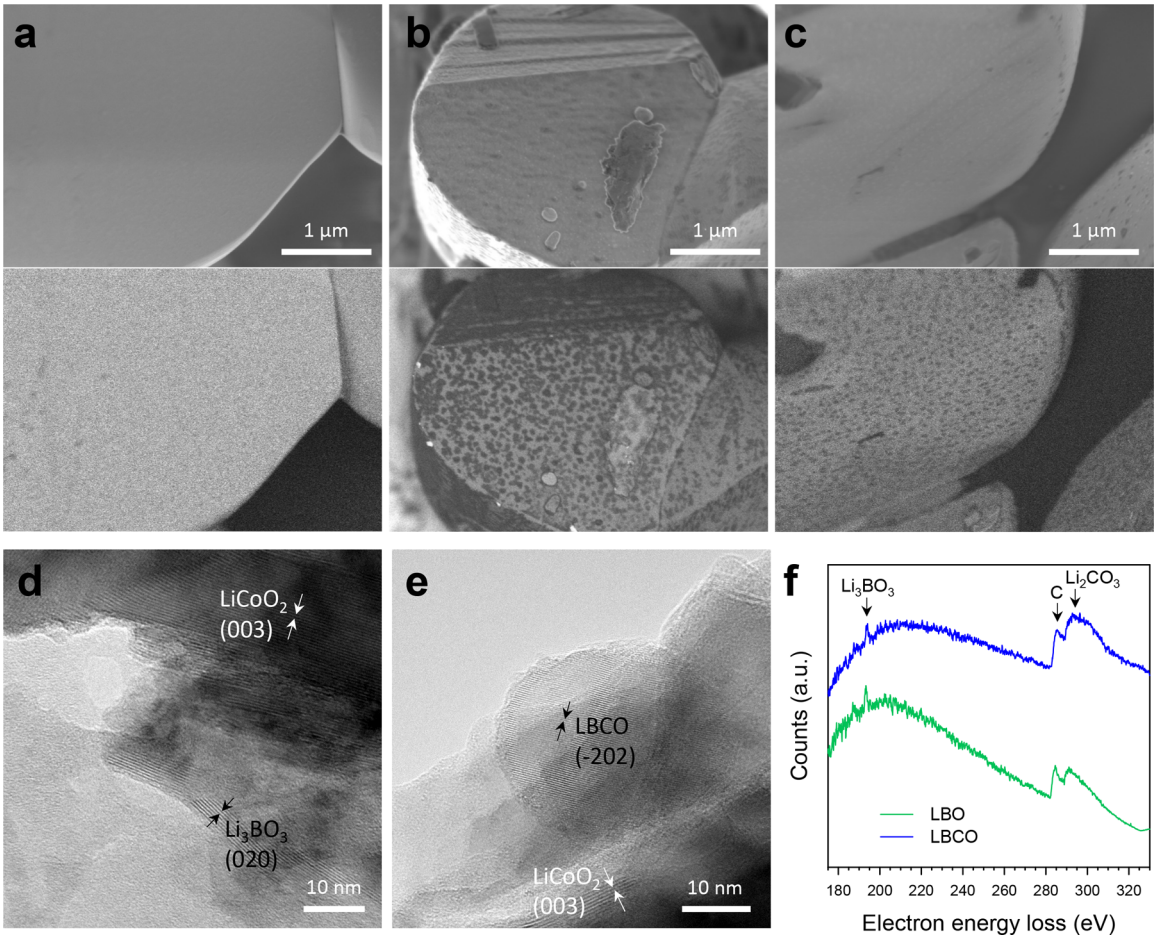

Figure 3. Characterization of c-bare (cleaned bare), LBO-coated (0.5 wt %), and LBCO-coated (0.5 wt % of LBO) $LiCoO_2$ by electron microscopy analysis. FESEM (upper) and the corresponding BSE (lower) images for (a) c-bare, (b) LBO-coated, and (c) LBCO-coated $LiCoO_2$ particles. HRTEM images for (d) LBO- and (e) LBCO-coated $LiCoO_2$ particles. (f) EELS for LBO- and LBCO-coated $LiCoO_2$ particles. The corresponding HRTEM images are provided in Figure S3a,b.

materials (Table S2). It is also expected that the practical cathodic limits of LBO and LBCO could be extended due to the sluggish kinetics of gas evolution reactions.[28,30] However, it should be noted that decomposition reactions at interfaces can originate from the chemical potential difference of elements other than Li.

Therefore, we further probed the interfacial stability between the cathode and SE material, along with the effects of applying coating materials on it. Various possible reactions at the interfaces before and after introducing coating materials were probed by calculating the thermodynamic reaction energies, as illustrated in Figure 1. The blue dashed line in the figure presents the interfacial reaction energy as a function of the phase fraction of the SE materials (LPSCl) surrounding the cathode ($LiCoO_2$), which models the various local compositional inhomogeneities in the composite electrode. These analyses reveal that the interface between the cathode and SE material is not thermodynamically stable but undergoes a

DOI: 10.1021/acs.chemmater.8b03321
Chem. Mater. 2018, 30, 8190−8200

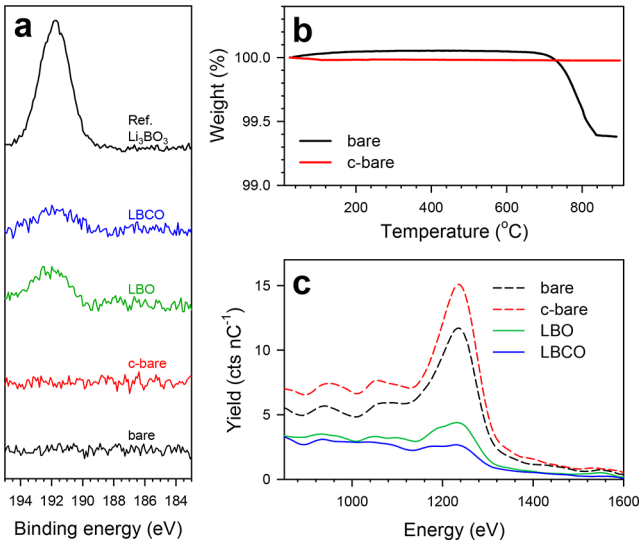

Figure 4. Characterization of bare, c-bare, LBO-coated, and LBCO-coated $LiCoO_2$. (a) XPS spectra for B 1s signals. (b) TGA profiles for bare and c-bare $LiCoO_2$ in N_2. (c) LEIS spectra for 5 keV Ne^+ incident ions.

spontaneous decomposition with negative reaction energy, which becomes maximum (−320 meV atom^{-1}) when LPSCl and $LiCoO_2$ react at a ratio of approximately 1:1. Moreover, the decomposition reaction is further promoted when the SE materials are in contact with the delithiated cathode ($Li_{0.5}CoO_2$), with a maximum energy of −450 meV atom^{-1}, as displayed by the red dashed line, indicating more serious side reactions during the charging of ASLBs. This decomposition reaction deteriorates the interface properties and often leads to an increase of cell impedance and the loss of active materials in the electrochemical reaction. However, we observed that the stability of the SE can be significantly enhanced when it is alternatively in contact with coating materials, such as LBCO or LBO. The solid lines show that the decomposition of electrolytes can be mitigated by coating layers with a substantially reduced reaction energy. Even though the decomposition reaction is still thermodynamically favorable, the driving force is reduced by less than one-fifth. Moreover, the interfaces between $LiCoO_2$ and LBCO (or LBO) were found to be stable without decomposition or with negligible decomposition energies (Table S3), which indicates that the surface degradation of $LiCoO_2$ can be suppressed by incorporating LBCO (or LBO) as coating layers. As a result, the incorporation of LBCO (or LBO) as a coating layer is expected to suppress the decomposition reactions of both the cathode and the SE materials at the interface of them.

Inspired by the computational results, a series of LBCO-coated $LiCoO_2$ samples were prepared, along with the reference samples of $Li_{3-x}B_{1-x}C_xO_3$. The reference $Li_{3-x}B_{1-x}C_xO_3$ samples were obtained from a homogeneous aqueous solution containing LiOH, H_3BO_3, and Li_2CO_3. The phase-pure LBO samples (JCPDS no. 18-0718, Figure S1a) exhibited a Li^+ conductivity of 1.4×10^{-9} S cm^{-1} at 30 °C (Figure S1b, Table S4).[52] As Li_2CO_3 is added into LBO, the characteristic peaks for the isostructural phase with Li_2CO_3 (JCPDS no. 22-1141) evolved, as seen in the XRD patterns (Figure S1a).[52,54] Correspondingly, Li^+ conductivity was drastically increased to 6.0×10^{-7} S cm^{-1} at $x = 0.80$ (Figure S1b, Table S4), which is comparable to that of the state-of-the-art coating material for sulfide ASLBs: amorphous $LiNbO_3$ (Table S1).[11,12,42]

LBO-coated $LiCoO_2$ was fabricated using surface-cleaned $LiCoO_2$, referred to as "c-bare", which was obtained by a heat treatment at 600 °C in air, while the LBCO-coated $LiCoO_2$ was obtained using impurity-containing bare $LiCoO_2$, referred to as "bare". The schematic diagram illustrating bare, c-bare, LBO-coated, and LBCO-coated $LiCoO_2$ is shown in Figure 2. Also, the characteristics of the LBO and LBCO coatings (weight fraction, thickness, and surface coverage) are provided in Table 1. Field emission scanning electron microscopy (FESEM) images of c-bare, LBO-coated (0.5 wt %), and LBCO-coated (0.5 wt % of LBO or 1.72 wt % of LBCO) $LiCoO_2$ particles (Figure 3a−c, S2) showed no noticeable differences. (Note: weight fraction of the coatings and x in in $Li_{3-x}B_{1-x}C_xO_3$ indicate targeting values, unless otherwise stated) However, the corresponding backscattered scanning electron (BSE) images reveal the inhomogeneous distribution of contrast in atomic numbers (Figure 3a−c, S2), confirming the presence of the coating layers for LBO- and LBCO-coated $LiCoO_2$. Although a direct observation of the coating layers by high-resolution transmission electron microscopy (HRTEM) was hindered by the vulnerability of the low atomic number constituents to electron beams, HRTEM images for LBO- and LBCO-coated $LiCoO_2$ particles showed lattice fringes corresponding with LBO ((020) plane) and likely LBCO ((−202) plane), as shown in Figure 3d,e, respectively. Moreover, the presence of boron in the form of Li_3BO_3 on the surface of LBO- and LBCO-coated $LiCoO_2$ was corroborated by scanning TEM (STEM) images (Figure S3) and their corresponding electron energy loss spectroscopy (EELS) peaks at ∼193 eV (Figure 3f).[55] In addition, compared with LBO-coated $LiCoO_2$, LBCO-coated $LiCoO_2$ exhibited a stronger carbon signature centered at ∼292 eV.[56]

The presence of boron in coated $LiCoO_2$ was also confirmed by X-ray photoelectron spectroscopy (XPS) data for B 1s signals (Figure 4a). Both LBO- and LBCO-coated $LiCoO_2$ samples showed peaks at 191.5 eV corresponding to B^{3+} for Li_3BO_3.[55] The surface impurity on $LiCoO_2$, Li_2CO_3, was quantified by thermogravimetric analysis (TGA) in N_2. Whereas the c-bare sample showed no weight loss up to 850 °C, the bare sample started to lose weight at 700 °C, which is indicative of the thermal decomposition of Li_2CO_3 (Figure 4b).[57] From the weight loss value, the amount of Li_2CO_3 on the surface of the bare sample was determined to be 1.1 wt %. The thicknesses of the coating layers were estimated considering the surface area of $LiCoO_2$ powders obtained by N_2 adsorption−desorption isotherm measurements and are given in Table 1. Low-energy ion scattering (LEIS) measurements were carried out to analyze the conformality of the coating layers on $LiCoO_2$.[58] In LEIS, low-energy backscattered ions are analyzed, allowing the identification and quantification of the elements in the outermost atomic layer of a substrate.[59] Figure 4c shows the LEIS spectra for bare, c-bare, LBO-coated (0.5 wt %), and LBCO-coated (0.5 wt % of LBO) $LiCoO_2$ particles when using 5 keV Ne^+ as incident ions. The strong peaks found at 1230 eV for the bare and c-bare samples correspond with the ions backscattered by Co in $LiCoO_2$. The lower intensity of the Co peak obtained for the bare sample compared with that obtained for the c-bare sample is due to surface impurities containing Li_2CO_3. Furthermore, the LBO- and LBCO-coated samples showed a much more attenuated Co-peak, indicating that Co atoms are well covered by the

DOI: 10.1021/acs.chemmater.8b03321
Chem. Mater. 2018, 30, 8190−8200

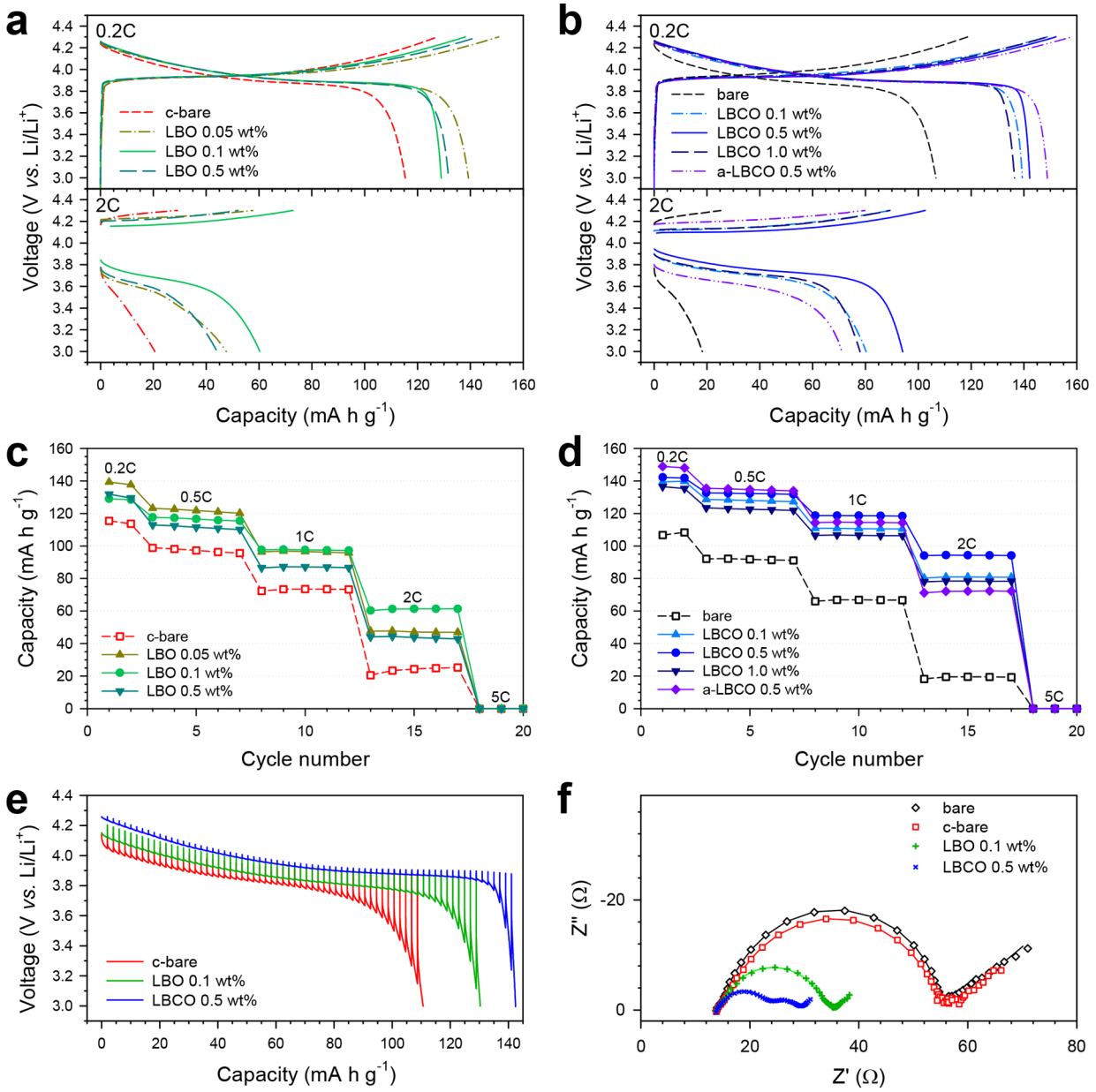

Figure 5. Electrochemical characterization of $LiCoO_2$/Li−In all-solid-state cells at 30 °C. Charge−discharge voltage profiles for (a) LBO- and (b) LBCO-coated $LiCoO_2$. Rate performances for (c) LBO- and (d) LBCO-coated $LiCoO_2$. The results for c-bare, bare, and a-LBCO-coated (artificial-LBCO-coated) $LiCoO_2$ are compared in (a−d). (e) Transient discharge voltage profiles obtained by GITT. (f) Nyquist plots of $LiCoO_2$/Li−In cells. The corresponding equivalent circuit model and interfacial resistances are shown in Figure S4 and Table S5, respectively.

coating layers. Assuming that the surfaces of the c-bare sample are perfectly uncovered, the surface coverages of the other samples were determined by comparing the intensities of the Co peaks and are shown in Table 1. For the bare sample, 21% of the surface is covered by impurities, such as Li_2CO_3. The surface coverages for LBO- and LBCO-coated samples turned out to be 79% and 87%, respectively. The higher surface coverage found for the LBCO-coated sample than for the LBO-coated one is attributed to the overall larger amount of coating materials.

The electrochemical performances of $LiCoO_2$/Li−In all-solid-state cells at 30 °C for LBO- and LBCO-coated $LiCoO_2$, depending on the weight fraction of the coatings, are shown in Figure 5 in comparison with those for the c-bare and bare samples. Compared with the c-bare $LiCoO_2$ samples, all the LBO-coated $LiCoO_2$ samples showed a lowered polarization in their charge−discharge voltage profiles (Figure 5a) and correspondingly higher capacities, especially at higher C-rates (Figure 5c), confirming the positive effect of the LBO coatings. The optimal performance obtained with 0.1 wt % of LBO may reflect that an interplay between the lowered direct contact of $LiCoO_2$-LPSCl and the nonimpeded Li^+ transport through the LBO coating determines the overall kinetics.[60,61] The electrochemical performance was further improved by the LBCO-coating (Figure 5b,d). $LiCoO_2$ coated with LBCO with 0.5 wt % of LBO exhibited the highest discharge capacities of 142 and 94 mA h g^{-1} at 0.2 and 2C, respectively, which are comparable to those of state-of-the-art $LiCoO_2$ electrodes in ASLBs.[11,12,34] It should be noted that the higher Li^+ conductivity of LBCO compared with that of LBO allows a larger amount of coatings

DOI: 10.1021/acs.chemmater.8b03321
Chem. Mater. 2018, 30, 8190−8200

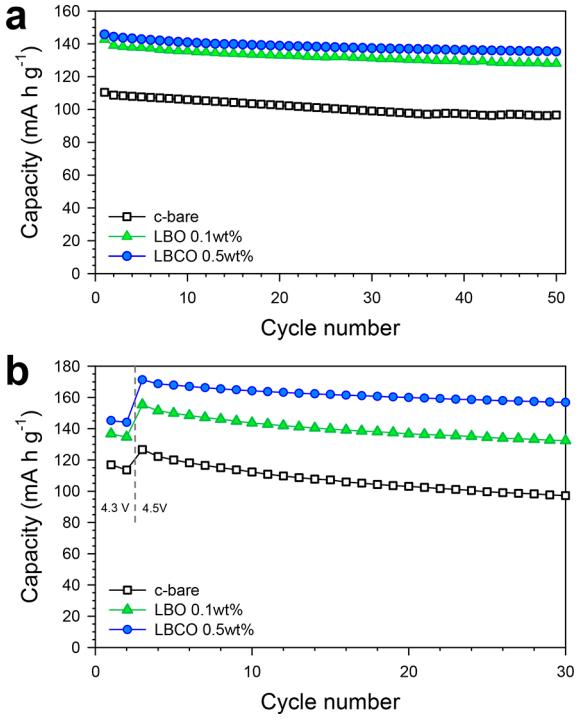

Figure 6. Cycling performances for $LiCoO_2$/Li−In all-solid-state cells using c-bare, LBO-coated, and LBCO-coated $LiCoO_2$ at 0.2C and 30 °C. Discharge capacities as a function of the number of cycles in the voltage ranges of (a) 3.0−4.3 V (vs Li/Li^+) and (b) 3.0−4.5 V (vs Li/Li^+).

to achieve an optimal rate capability (Table S1). LBCO coating was also applied on c-bare $LiCoO_2$ using an aqueous solution containing LiOH, H_3BO_3, and Li_2CO_3; this sample is referred to as artificial LBCO-coated $LiCoO_2$ (a-LBCO). Consistent with the results of LBCO-coated $LiCoO_2$, a-LBCO-coated $LiCoO_2$ also showed an excellent rate capability. The trend of improvement, which goes in the order of bare (or c-bare), LBO-coated, and LBCO-coated samples, agrees well with the lowered polarization in the transient discharge voltage profiles obtained by galvanostatic intermittent titration technique (GITT) (Figure 5e) and the smaller interfacial resistances obtained from Nyquist plots (Figures 5f and S4 and Table S5).

The cycling performances of $LiCoO_2$/Li−In all-solid-state cells at 0.2C and 30 °C using c-bare, LBO-coated, and LBCO-coated $LiCoO_2$ are shown in Figure 6. With an upper cutoff voltage of 4.3 V (vs. Li/Li^+), the capacity retention for c-bare samples after 50 cycles, compared with that at the second cycle, was 88.8%. The coatings of LBO (0.1 wt %) and LBCO (0.5 wt % LBO) resulted in enhancements in capacity retention: 92.2% and 93.8%, respectively. When the upper cutoff voltage was raised to 4.5 V (vs Li/Li^+), more dramatic improvements in cycling performance caused by the coating were confirmed; the capacity retentions after 25 cycles, compared with that at the fourth cycle, were 81.6%, 88.7%, and 93.8% for c-bare, LBO-coated, and LBCO-coated $LiCoO_2$, respectively. Notably, the electrochemical performance of LBCO-coated $LiCoO_2$ for ASLBs appears to be superior to even that of the $LiNbO_3$-coated sample (Figure S5). From the electrochemical results, the following features are summarized: (i) the rate capability and cycling performances are enhanced, from worst to best, in the order of bare (or c-bare), LBO-coated, and LBCO-coated $LiCoO_2$, and (ii) compared with LBO coatings, thicker coatings are possible using LBCO thanks to its higher Li^+ conductivity.

As an attempt to gain mechanistic insights on the protective coatings on $LiCoO_2$ for ASLBs, ex situ XPS analyses were carried out for c-bare, LBO-coated, and LBCO-coated $LiCoO_2$ electrodes before and after cycling to probe for changes at the electrode−SE interfaces. Because the mixture electrodes do not contain conducting carbon additives, any effects caused by carbon-SE interfaces could be ruled out. The signals for Co 2p, S 2p, and P 2p are shown in Figure 7. For the Co 2p spectra shown in Figure 7a, the evolution of Co_3S_4 after cycling (shown in the deconvoluted peaks in violet) is noticeable.[62,63] Because the physical mixture sample of c-bare $LiCoO_2$/LPSCl does not show the signature of Co_3S_4, the formation of Co_3S_4 is suspected to be electrochemically driven, which is consistent with the observation of interatomic diffusion of Co and S at the interfaces of $LiCoO_2/Li_2S{\cdot}P_2S_5$ presented in a previous report.[34] Because Co_3S_4 is electronically conducting (thus nonpassivating), reactions at bare $LiCoO_2$/LPSCl interfaces occur progressively, which is detrimental to their electrochemical performance.[28,29,32] In stark contrast, the Co 2p signal for LBO-coated $LiCoO_2$ after cycling shows a much lower intensity for Co_3S_4. Moreover, LBCO-coated $LiCoO_2$ after cycling showed a negligible signature of Co_3S_4. This result reflects the excellent protection of $LiCoO_2$ provided by LBCO, which can be attributed to its high surface coverage (Figure 4c, Table 1) and its buffering effects, as our first-principles computational results suggest (Table S3). In a consistent fashion, the suppressed evolution of Co_3S_4 after cycling from worst to best was confirmed to be in the order of c-bare, LBO-coated, and LBCO-coated $LiCoO_2$, as shown by the S 2p signals in Figure 7b. As shown in the P 2p signals in Figure 7c, the signature of phosphate (PO_4^{3-}, shown in the deconvoluted peaks in dark cyan) appeared for the LBO-coated sample and became more intense for the LBCO-coated one.[46,64] The phosphate species could be derived from the electrochemical reaction of LBO or LBCO with LPSCl. In contrast to Co_3S_4, the as-formed phosphates are good electronic insulators, thus effectively passivating to inhibit the continuous decomposition of the bulk SEs.[28,29,32] The evolution of bridging sulfur (S−S or P−$[S]_n$−P ($n \geq 2$) after cycling observed in the S 2p and P 2p signals is consistent with previous reports.[46,65,66]

Based on the electrochemical characterization and the complementary analyses presented so far, the interface phases between cathode and SE material appear to be sensitively dependent on the coating materials used, as illustrated in Figure 8. The surfaces of bare $LiCoO_2$ are covered by the impurities, including Li_2CO_3. More importantly, the electrochemically driven reactions between $LiCoO_2$ and LPSCl form detrimental mixed conducting interphases (MCIs), as evidenced by the observation of Co_3S_4, which shows a lack of passivating capability. The aqueous-solution coating process for LBO renders to form the LBCO layers. The high Li^+ conductivity of LBCO allows for the formation of thick and thus high-surface-coverage protective layers, which suppresses the significant decomposition at the interface. Moreover, the electrochemical reaction of LBCO with LPSCl enables the formation of good passivating layers comprised of phosphates. As an overall consequence, LBCO coating on $LiCoO_2$ results in significant improvements in rate capability and durability.

DOI: 10.1021/acs.chemmater.8b03321
Chem. Mater. 2018, 30, 8190−8200

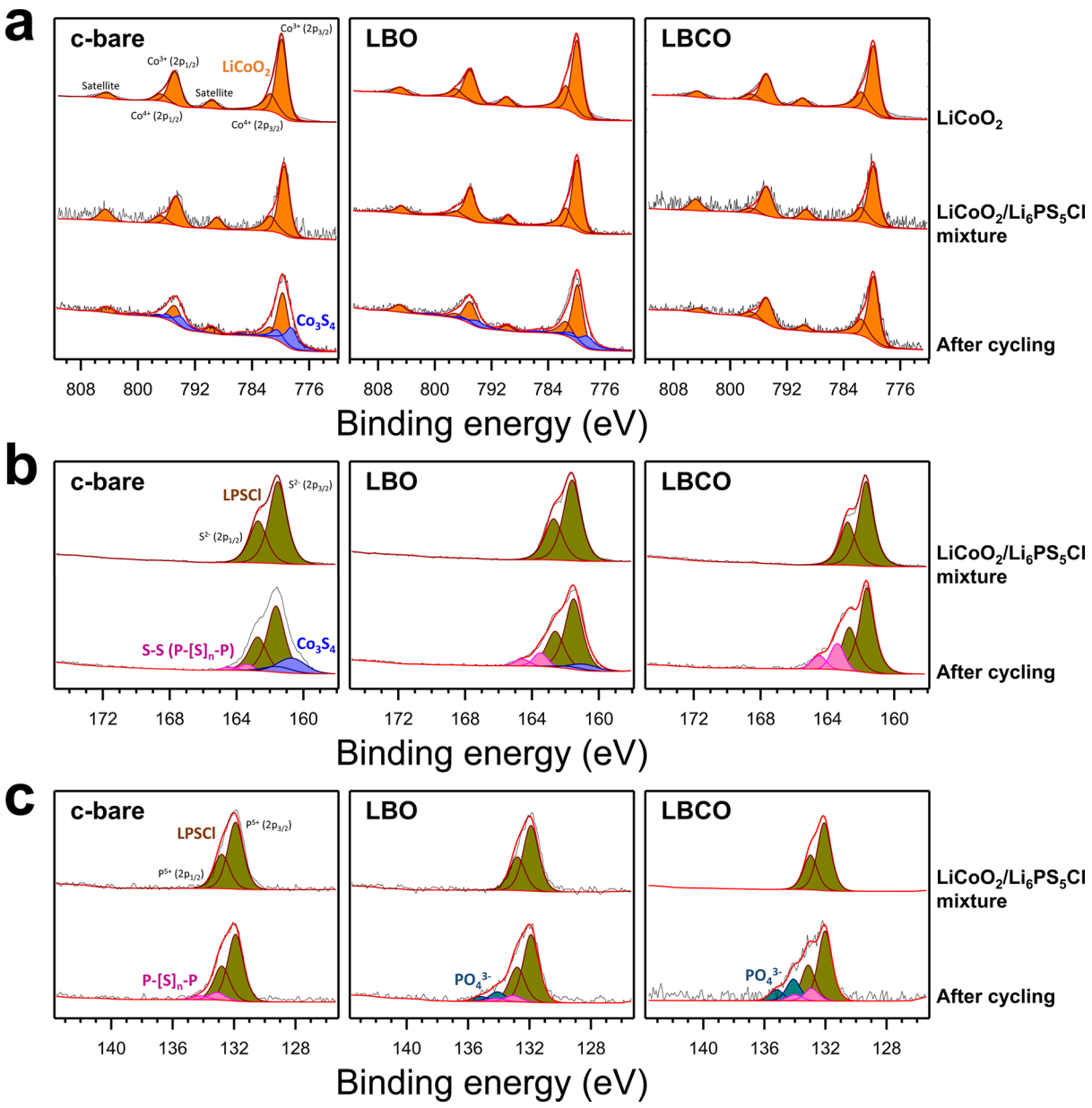

Figure 7. XPS results for c-bare, LBO-coated (0.1 wt %), and LBCO-coated (0.5 wt % of LBO) $LiCoO_2$ for pristine powders and electrodes after cycling. The data for $LiCoO_2$/SE (Li_6PS_5Cl) mixtures are also shown for comparison. The signals for (a) Co 2p, (b) S 2p, and (c) P 2p are shown.

CONCLUSION

In summary, a new LBCO coating process on $LiCoO_2$ for sulfide-based ASLBs via a scalable aqueous-solution protocol was rationally designed, considering the formation of an interphase between the cathode and SE materials, and was demonstrated to significantly improve electrochemical performances. Using the aforementioned aqueous LBO-solution process, the poorly Li^+-conducting surface impurity on $LiCoO_2$, Li_2CO_3, could be converted into highly Li^+-conductive LBCO (max. conductivity of 6.0×10^{-7} S cm^{-1} at 30 °C), which could protect $LiCoO_2$ with thick and high-surface-coverage layers. More specifically, $LiCoO_2$/Li−In all-solid-state cells employing the proposed LBCO coating with 0.5 wt % LBO showed discharge capacities of 142 and 94 mA h g^{-1} at 30 °C at 0.2C and 2C, respectively, in contrast to the discharge capacities of 107 and 18 mA h g^{-1} obtained for the ones using bare $LiCoO_2$. From the complementary analyses by electrochemical measurements, XRD, FESEM, BSE, HRTEM, EELS, TGA, LEIS, and ex situ XPS, it was revealed that the LBCO coatings prevent the evolution of detrimental MCIs containing Co_3S_4 and can effectively passivate the interfaces by alternatively forming phosphate-based phases. We believe that our results not only provide an in-depth mechanistic understanding on the interfacial evolutions for ASLBs but also open up a new avenue to rationally engineer the interfaces for practical all-solid-state technologies.

EXPERIMENTAL SECTION

Preparation of Materials. The LBO and LBCO powders were prepared by dissolving stoichiometric amounts of LiOH (99.995%, Alfa Aesar), H_3BO_3 (>99.5%, Sigma-Aldrich), and Li_2CO_3 (99.997%, Sigma-Aldrich) in deionized water. In order to minimize any effects of different precipitation kinetics for Li_2CO_3 and Li_3BO_3 (from H_3BO_3 and LiOH), the water was evaporated under a vacuum at 80 °C using a rotary evaporator, followed by a heat treatment at 600 °C for 5 h in

DOI: 10.1021/acs.chemmater.8b03321
Chem. Mater. 2018, 30, 8190−8200

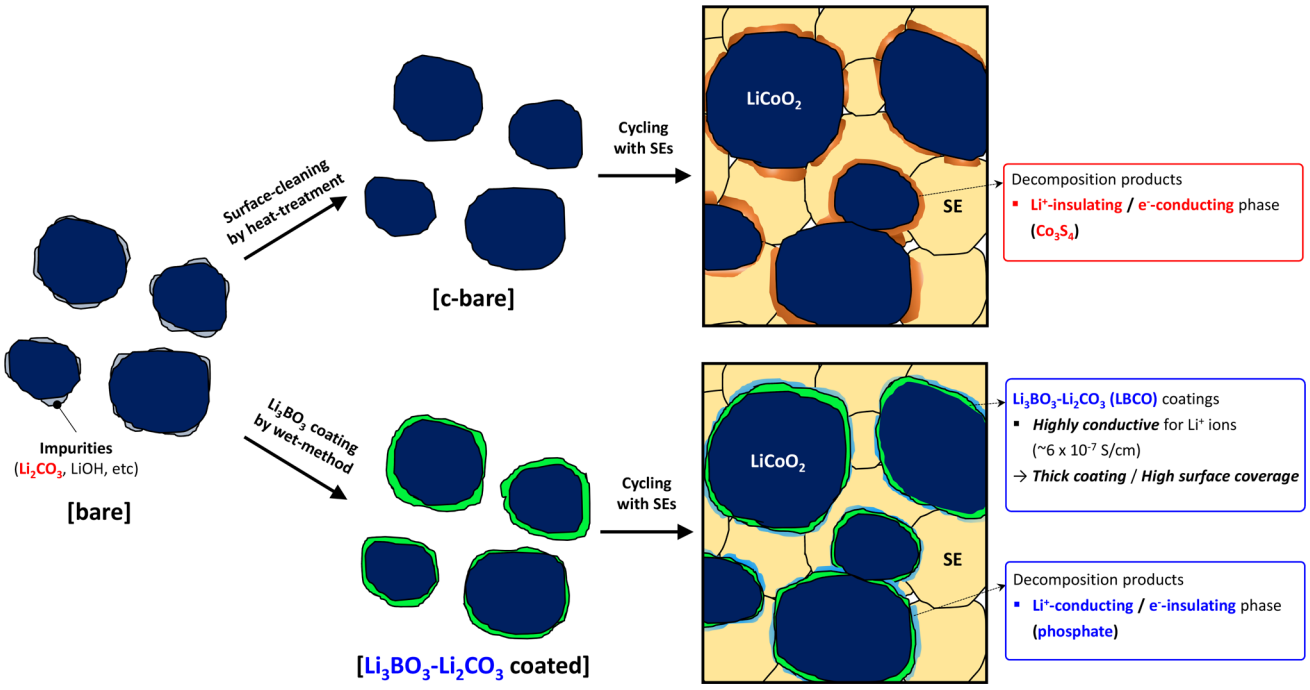

Figure 8. Schematic diagram illustrating the different interface features of bare and LBCO-coated $LiCoO_2$ in all-solid-state-cell electrodes.

air. The cleaned bare $LiCoO_2$ powders (c-bare) were prepared by heat treatment at 600 °C for 10 h in air. The LBO- and LBCO-coated $LiCoO_2$ powders were prepared using an aqueous LBO solution. After the bare $LiCoO_2$ powders were added into the coating solution prepared by dissolving a stoichiometric amount of LiOH (99.995%, Alfa Aesar) and H_3BO_3 (>99.5%, Sigma-Aldrich) in deionized water, the solvent was evaporated under a vacuum at 80 °C using a rotary evaporator, followed by a heat treatment at 600 °C for 10 h in air. To obtain the LBO- and LBCO-coated $LiCoO_2$ powders, c-bare and bare $LiCoO_2$ powders were used, respectively. For the LBCO-coated $LiCoO_2$ powders, the surface impurity, Li_2CO_3, serves as the source for the coating materials. In contrast, the artificial-LBCO-coated (a-LBCO) $LiCoO_2$ powders were prepared using c-bare $LiCoO_2$ and a coating solution, prepared by dissolving LiOH, H_3BO_3, and Li_2CO_3 (99.997%, Sigma-Aldrich) in deionized water. The LPSCl SE powders were prepared by ball milling a stoichiometric mixture of Li_2S (99.9%, Alfa Aesar), P_2S_5 (99%, Sigma-Aldrich), and LiCl (99.99%, Sigma-Aldrich) at 600 rpm for 10 h with ZrO_2 balls.[23] Then, the ball-milled powders were heat-treated at 550 °C for 5 h in an Ar atmosphere.

Thermodynamic Calculations. Intrinsic electrochemical windows were predicted by constructing Li grand potential phase diagrams.[28,30,31] Potential reactions at the interfaces were considered as chemical reactions between two corresponding compositions at the interfaces.[30,31] Multidimensional compositional phase diagrams were constructed, and then pseudobinary phase diagrams that have the two target compositions as end points were extracted from the multidimensional phase diagrams. The potential decomposition reactions were examined along the pseudobinary phase diagrams with varying fractions of reactants. Most of the energy values used for constructing phase diagrams were obtained from the Materials Project database.[67] However, the energies of unstable target materials, such as layered $Li_{0.5}CoO_2$ and Li_6PS_5Cl, were corrected by making their decomposition energies become zero, as previously suggested.[28] Additionally, the energy of LBCO ($Li_{3-x}B_{1-x}C_xO_3$, x = 0.80) was evaluated as a linear combination of Li_3BO_3 and Li_2CO_3 because calculating the exact energy of the phase is computationally impossible. Despite these assumptions, we believe that the error of the calculated decomposition energy does not significantly affect the outcome of this study.

Materials Characterization. The XRD measurements were conducted using a D8-Bruker Advance diffractometer under Cu Kα radiation (1.54056 Å). To avoid exposure to air, the samples were sealed with a Be window. The FESEM and BSE measurements were carried out using Quanta 200FEG (FEI). The accelerating voltage and emission current were fixed at 1 kV and 10.5 μA, respectively. The HRTEM images and their corresponding selected-area electron diffraction (SAED) patterns and EELS spectra were obtained using JEM-2100 (JEOL) and JEM-2100F (JEOL). The XPS data were collected with a monochromatic Al Kα source (1486.6 eV) at 72 W, 12 kV, and 6 mA using an X-ray photoelectron spectrometer (ThermoFisher). For the ex situ XPS measurements, the collected samples were loaded in an Ar-filled dry glovebox and loaded into the XPS equipment quickly while minimizing exposure to air. The amount of B was determined using inductively coupled plasma optical emission spectroscopy (ICP-OES, 720-ES, Varian). The amount of C in bare $LiCoO_2$ was obtained by the TGA measurements using Q500 (TA Instrument Corp) and applied to determine the amount of LBCO in LBCO-coated $LiCoO_2$. Also, the amount of C in LBCO-coated $LiCoO_2$ was directly measured using elemental analyzer (EA, FLASH EA1112). The LEIS measurements were carried out using Qtac100 (IONTOF GmbH).

Electrochemical Characterization. For the measurement of Li^+ conductivity, LBO and LBCO powders were prepared by the same procedure for preparing LBO- and LBCO-coated $LiCoO_2$, except for the presence of $LiCoO_2$. Then, the powders were pelletized by cold-pressing at 370 MPa and subsequent sintering at 600 °C for 5 h in air. The as-prepared pellets were subjected to measurements of Li^+ conductivity by the AC impedance method (Iviumstat, IVIUM Technologies Corp.) using symmetric Li-ion blocking carbon-coated Al (c-Al)/pellet/c-Al cells. The $LiCoO_2$/Li−In all-solid-state cells were prepared as follows.[12,23] Partially lithiated indium ($Li_{0.5}In$, nominal composition) powders were prepared by mechanically milling a mixture of In (Sigma-Aldrich, 99.99%) and Li (FMC Lithium corp.). After the SE layer was formed by pressing 150 mg of LPSCl powders, the electrode mixtures of $LiCoO_2$ and LPSCl (70:30 weight ratio) were spread on one side of the SE layer, followed by pressing. Then, the as-prepared $Li_{0.5}In$ powders were put on the other side of the SE layer. Finally, the whole assemblies were pressed at 370 MPa. The mass loading of $LiCoO_2$ was 8.3 mg cm^{-2}. All the pressing was carried out in a polyaryletheretherketone (PEEK) mold (diameter = 13 mm) with Ti rods as current collectors. All the electrochemical tests were conducted at 30 °C. The C-rate of 1C corresponds with

DOI: 10.1021/acs.chemmater.8b03321
Chem. Mater. 2018, 30, 8190−8200

161 mA g^{-1}. The GITT measurements were carried out at a pulse current of 0.5C for 90 s and a rest for 2 h. The EIS measurements were performed from 1.5 MHz to 5 mHz with 10 mV of amplitude after discharging the cells to 3.9 V (vs Li/Li^+) at 0.2C at the second cycle.

■ ASSOCIATED CONTENT

Supporting Information

The Supporting Information is available free of charge on the ACS Publications website at DOI: 10.1021/acs.chemmater.8b03321.

Characterization of coating materials and active materials (XRD, conductivity, SEM images, TEM images, thermodynamic properties) and additional electrochemical information (PDF)

■ AUTHOR INFORMATION

Corresponding Authors

*E-mail: yoonsjung@hanyang.ac.kr (Y. S. Jung).
*E-mail: maltgen1@snu.ac.kr (K. Kang).

ORCID

Kisuk Kang: 0000-0002-8696-1886
Yoon Seok Jung: 0000-0003-0357-9508

Author Contributions

S.H.J. and K.O. contributed equally.

Notes

The authors declare no competing financial interest.

■ ACKNOWLEDGMENTS

This research was supported by Hyundai Motors, by the Technology Development Program to Solve Climate Changes and by Basic Science Research Program of the National Research Foundation (NRF) funded by the Ministry of Science & ICT (Grant No. NRF-2017M1A2A2044501 and 2018R1A2B6004996), and by the Materials and Components Technology Development Program of MOTIE/KEIT (Grant No. 10077709).

■ REFERENCES

(1) Goodenough, J. B.; Kim, Y. Challenges for Rechargeable Li Batteries. *Chem. Mater.* **2010**, *22*, 587−603.
(2) Kalhoff, J.; Eshetu, G. G.; Bresser, D.; Passerini, S. Safer Electrolytes for Lithium-Ion Batteries: State of the Art and Perspectives. *ChemSusChem* **2015**, *8*, 2154−2175.
(3) Choi, J. W.; Aurbach, D. Promise and reality of post-lithium-ion batteries with high energy densities. *Nat. Rev. Mater.* **2016**, *1*, 16013.
(4) Spotnitz, R.; Franklin, J. Abuse behavior of high-power, lithium-ion cells. *J. Power Sources* **2003**, *113*, 81−100.
(5) Jung, Y. S.; Cavanagh, A. S.; Gedvilas, L.; Widjonarko, N. E.; Scott, I. D.; Lee, S. H.; Kim, G. H.; George, S. M.; Dillon, A. C. Improved Functionality of Lithium-Ion Batteries Enabled by Atomic Layer Deposition on the Porous Microstructure of Polymer Separators and Coating Electrodes. *Adv. Energy Mater.* **2012**, *2*, 1022−1027.
(6) Wu, H.; Zhuo, D.; Kong, D. S.; Cui, Y. Improving battery safety by early detection of internal shorting with a bifunctional separator. *Nat. Commun.* **2014**, *5*, 5193.
(7) Yamada, Y.; Usui, K.; Sodeyama, K.; Ko, S.; Tateyama, Y.; Yamada, A. Hydrate-melt electrolytes for high-energy-density aqueous batteries. *Nat. Energy* **2016**, *1*, 16129.
(8) Suo, L. M.; Hu, Y. S.; Li, H.; Armand, M.; Chen, L. Q. A new class of Solvent-in-Salt electrolyte for high-energy rechargeable metallic lithium batteries. *Nat. Commun.* **2013**, *4*, 1481.
(9) Woollaston, V. New blow for Tesla: Fire in the 'world's safest electric car' began in vehicle's battery. http://www.dailymail.co.uk/sciencetech/article-2442392/New-blow-Tesla-Fire-worlds-safest-electric-car-began-vehicles-battery.html (accessed October 16th, 2018).
(10) Park, K. H.; Bai, Q.; Kim, D. H.; Oh, D. Y.; Zhu, Y.; Mo, Y.; Jung, Y. S. Design Strategies, Practical Considerations, and New Solution Processes of Sulfide Solid Electrolytes for All-Solid-State Batteries. *Adv. Energy Mater.* **2018**, *8*, 1800035.
(11) Kato, Y.; Hori, S.; Saito, T.; Suzuki, K.; Hirayama, M.; Mitsui, A.; Yonemura, M.; Iba, H.; Kanno, R. High-power all-solid-state batteries using sulfide superionic conductors. *Nat. Energy* **2016**, *1*, 16030.
(12) Park, K. H.; Oh, D. Y.; Choi, Y. E.; Nam, Y. J.; Han, L.; Kim, J.-Y.; Xin, H.; Lin, F.; Oh, S. M.; Jung, Y. S. Solution-Processable Glass LiI-Li_4SnS_4 Superionic Conductors for All-Solid-State Li-Ion Batteries. *Adv. Mater.* **2016**, *28*, 1874−1883.
(13) Banerjee, A.; Park, K. H.; Heo, J. W.; Nam, Y. J.; Moon, C. K.; Oh, S. M.; Hong, S.-T.; Jung, Y. S. Na_3SbS_4A Solution Processable Sodium Superionic Conductor for All-Solid-State Sodium-Ion Batteries. *Angew. Chem., Int. Ed.* **2016**, *55*, 9634−9638.
(14) Heo, J. W.; Banerjee, A.; Park, K. H.; Jung, Y. S.; Hong, S.-T. Na-ion Solid Electrolytes $Na_{4-x}Sn_{1-x}Sb_xS_4$ ($0.02 < x < 0.33$) for All-Solid-State Na-ion Batteries. *Adv. Energy Mater.* **2018**, *8*, 1702716.
(15) Moon, C. K.; Lee, H.-J.; Park, K. H.; Kwak, H.; Heo, J. W.; Choi, K.; Yang, H.; Kim, M.-S.; Hong, S.-T.; Lee, J. H.; Jung, Y. S. Vacancy-Driven Na^+ Superionic Conduction in New Ca-Doped Na_3PS_4 for All-Solid-State Na-Ion Batteries. *ACS Energy Lett.* **2018**, *3*, 2504−2512.
(16) Jung, Y. S.; Oh, D. Y.; Nam, Y. J.; Park, K. H. Issues and Challenges for Bulk-Type All-Solid-State Rechargeable Lithium Batteries using Sulfide Solid Electrolytes. *Isr. J. Chem.* **2015**, *55*, 472−485.
(17) Janek, J.; Zeier, W. G. A solid future for battery development. *Nat. Energy* **2016**, *1*, 16141.
(18) Albertus, P.; Babinec, S.; Litzelman, S.; Newman, A. Status and challenges in enabling the lithium metal electrode for high-energy and low-cost rechargeable batteries. *Nat. Energy* **2018**, *3*, 16−21.
(19) Kerman, K.; Luntz, A.; Viswanathan, V.; Chiang, Y.-M.; Chen, Z. Review-Practical Challenges Hindering the Development of Solid State Li Ion Batteries. *J. Electrochem. Soc.* **2017**, *164*, A1731−A1744.
(20) Manthiram, A.; Yu, X.; Wang, S. Lithium battery chemistries enabled by solid-state electrolytes. *Nat. Rev. Mater.* **2017**, *2*, 16103.
(21) Han, X.; Gong, Y.; Fu, K. K.; He, X.; Hitz, G. T.; Dai, J.; Pearse, A.; Liu, B.; Wang, H.; Rubloff, G.; Mo, Y.; Thangadurai, V.; Wachsman, E. D.; Hu, L. Negating interfacial impedance in garnet-based solid-state Li metal batteries. *Nat. Mater.* **2017**, *16*, 572−579.
(22) Kamaya, N.; Homma, K.; Yamakawa, Y.; Hirayama, M.; Kanno, R.; Yonemura, M.; Kamiyama, T.; Kato, Y.; Hama, S.; Kawamoto, K.; Mitsui, A. A lithium superionic conductor. *Nat. Mater.* **2011**, *10*, 682−686.
(23) Seino, Y.; Ota, T.; Takada, K.; Hayashi, A.; Tatsumisago, M. A sulphide lithium super ion conductor is superior to liquid ion conductors for use in rechargeable batteries. *Energy Environ. Sci.* **2014**, *7*, 627−631.
(24) Doyle, M.; Fuller, T. F.; Newman, J. THE IMPORTANCE OF THE LITHIUM ION TRANSFERENCE NUMBER IN LITHIUM POLYMER CELLS. *Electrochim. Acta* **1994**, *39*, 2073−2081.
(25) Nam, Y. J.; Oh, D. Y.; Jung, S. H.; Jung, Y. S. Toward practical all-solid-state lithium-ion batteries with high energy density and safety: Comparative study for electrodes fabricated by dry- and slurry-mixing processes. *J. Power Sources* **2018**, *375*, 93−101.
(26) Sakuda, A.; Hayashi, A.; Tatsumisago, M. Sulfide Solid Electrolyte with Favorable Mechanical Property for All-Solid-State Lithium Battery. *Sci. Rep.* **2013**, *3*, 2261.
(27) Nam, Y. J.; Park, K. H.; Oh, D. Y.; An, W. H.; Jung, Y. S. Diagnosis of Failure Modes for All-Solid-State Li-ion Batteries Enabled by Three-Electrode Cells. *J. Mater. Chem. A* **2018**, *6*, 14867−14875.

(28) Zhu, Y.; He, X.; Mo, Y. Origin of Outstanding Stability in the Lithium Solid Electrolyte Materials: Insights from Thermodynamic Analyses Based on First-Principles Calculations. *ACS Appl. Mater. Interfaces* **2015**, *7*, 23685−23693.
(29) Wenzel, S.; Leichtweiss, T.; Weber, D. A.; Sann, J.; Zeier, W. G.; Janek, J. Interfacial Reactivity Benchmarking of the Sodium Ion Conductors Na_3PS_4 and Sodium β-Alumina for Protected Sodium Metal Anodes and Sodium All-Solid-State Batteries. *ACS Appl. Mater. Interfaces* **2016**, *8*, 28216−28224.
(30) Zhu, Y.; He, X.; Mo, Y. First principles study on electrochemical and chemical stability of solid electrolyte-electrode interfaces in all-solid-state Li-ion batteries. *J. Mater. Chem. A* **2016**, *4*, 3253−3266.
(31) Richards, W. D.; Miara, L. J.; Wang, Y.; Kim, J. C.; Ceder, G. Interface Stability in Solid-State Batteries. *Chem. Mater.* **2016**, *28*, 266−273.
(32) Tian, Y. S.; Shi, T.; Richards, W. D.; Li, J. C.; Kim, J. C.; Bo, S. H.; Ceder, G. Compatibility issues between electrodes and electrolytes in solid-state batteries. *Energy Environ. Sci.* **2017**, *10*, 1150−1166.
(33) Nam, Y. J.; Cho, S.-J.; Oh, D. Y.; Lim, J.-M.; Kim, S. Y.; Song, J. H.; Lee, Y. G.; Lee, S.-Y.; Jung, Y. S. Bendable and Thin Sulfide Solid Electrolyte Film: A New Electrolyte Opportunity for Free-Standing and Stackable High-Energy All-Solid-State Lithium-Ion Batteries. *Nano Lett.* **2015**, *15*, 3317−3323.
(34) Sakuda, A.; Hayashi, A.; Tatsumisago, M. Interfacial Observation between $LiCoO_2$ Electrode and Li_2S-P_2S_5 Solid Electrolytes of All-Solid-State Lithium Secondary Batteries Using Transmission Electron Microscopy. *Chem. Mater.* **2010**, *22*, 949−956.
(35) Ohta, N.; Takada, K.; Zhang, L.; Ma, R.; Osada, M.; Sasaki, T. Enhancement of the high-rate capability of solid-state lithium batteries by nanoscale interfacial modification. *Adv. Mater.* **2006**, *18*, 2226−2229.
(36) Takada, K. Interfacial Nanoarchitectonics for Solid-State Lithium Batteries. *Langmuir* **2013**, *29*, 7538−7541.
(37) Kim, D. H.; Oh, D. Y.; Park, K. H.; Choi, Y. E.; Nam, Y. J.; Lee, H. A.; Lee, S.-M.; Jung, Y. S. Infiltration of Solution-Processable Solid Electrolytes into Conventional Li-Ion-Battery Electrodes for All-Solid-State Li-Ion Batteries. *Nano Lett.* **2017**, *17*, 3013−3020.
(38) Liu, H. S.; Zhang, Z. R.; Gong, Z. L.; Yang, Y. Origin of deterioration for $LiNiO_2$ cathode material during storage in air. *Electrochem. Solid-State Lett.* **2004**, *7*, A190−A193.
(39) Xiong, X. H.; Wang, Z. X.; Yue, P.; Guo, H. J.; Wu, F. X.; Wang, J. X.; Li, X. H. Washing effects on electrochemical performance and storage characteristics of $LiNi_{0.8}Co_{0.1}Mn_{0.1}O_2$ as cathode material for lithium-ion batteries. *J. Power Sources* **2013**, *222*, 318−325.
(40) Liu, W.; Oh, P.; Liu, X.; Lee, M. J.; Cho, W.; Chae, S.; Kim, Y.; Cho, J. Nickel-Rich Layered Lithium Transition-Metal Oxide for High-Energy Lithium-Ion Batteries. *Angew. Chem., Int. Ed.* **2015**, *54*, 4440−4457.
(41) Visbal, H.; Fujiki, S.; Aihara, Y.; Watanabe, T.; Park, Y.; Doo, S. The influence of the carbonate species on $LiNi_{0.8}Co_{0.05}O_2$ surfaces for all-solid-state lithium ion battery performance. *J. Power Sources* **2014**, *269*, 396−402.
(42) Ohta, N.; Takada, K.; Sakaguchi, I.; Zhang, L.; Ma, R.; Fukuda, K.; Osada, M.; Sasaki, T. $LiNbO_3$-coated $LiCoO_2$ as cathode material for all solid-state lithium secondary batteries. *Electrochem. Commun.* **2007**, *9*, 1486−1490.
(43) Xu, X.; Takada, K.; Fukuda, K.; Ohnishi, T.; Akatsuka, K.; Osada, M.; Hang, B. T.; Kumagai, K.; Sekiguchi, T.; Sasaki, T. Tantalum oxide nanomesh as self-standing one nanometre thick electrolyte. *Energy Environ. Sci.* **2011**, *4*, 3509−3512.
(44) Woo, J. H.; Travis, J. J.; George, S. M.; Lee, S.-H. Utilization of Al_2O_3 Atomic Layer Deposition for Li Ion Pathways in Solid State Li Batteries. *J. Electrochem. Soc.* **2015**, *162*, A344−A349.
(45) Ito, Y.; Sakurai, Y.; Yubuchi, S.; Sakuda, A.; Hayashi, A.; Tatsumisago, M. Application of $LiCoO_2$ Particles Coated with Lithium Ortho-Oxosalt Thin Films to Sulfide-Type All-Solid-State Lithium Batteries Batteries and Energy Storage. *J. Electrochem. Soc.* **2015**, *162*, A1610.
(46) Auvergniot, J.; Cassel, A.; Ledeuil, J. B.; Viallet, V.; Seznec, V.; Dedryvere, R. Interface Stability of Argyrodite Li6PS5Cl toward $LiCoO_2LiNi_{1/3}Co_{1/3}Mn_{1/3}O_2$ and $LiMn_2O_4$ in Bulk All-Solid-State Batteries. *Chem. Mater.* **2017**, *29*, 3883−3890.
(47) Koerver, R.; Aygün, I.; Leichtweiß, T.; Dietrich, C.; Zhang, W.; Binder, J. O.; Hartmann, P.; Zeier, W. G.; Janek, J. Capacity Fade in Solid-State Batteries: Interphase Formation and Chemomechanical Processes in Nickel-Rich Layered Oxide Cathodes and Lithium Thiophosphate Solid Electrolytes. *Chem. Mater.* **2017**, *29*, 5574−5582.
(48) Shannon, R. D.; Taylor, B. E.; English, A. D.; Berzins, T. NEW LI SOLID ELECTROLYTES. *Electrochim. Acta* **1977**, *22*, 783−796.
(49) Ohta, S.; Komagata, S.; Seki, J.; Saeki, T.; Morishita, S.; Asaoka, T. All-solid-state lithium ion battery using garnet-type oxide and Li_3BO_3 solid electrolytes fabricated by screen-printing. *J. Power Sources* **2013**, *238*, 53−56.
(50) Ohta, S.; Seki, J.; Yagi, Y.; Kihira, Y.; Tani, T.; Asaoka, T. Co-sinterable lithium garnet-type oxide electrolyte with cathode for all-solid-state lithium ion battery. *J. Power Sources* **2014**, *265*, 40−44.
(51) Okumura, T.; Takeuchi, T.; Kobayashi, H. All-solid-state lithium-ion battery using $Li_{2.2}C_{0.8}B_{0.2}O_3$ electrolyte. *Solid State Ionics* **2016**, *288*, 248−252.
(52) Nagao, K.; Hayashi, A.; Tatsumisago, M. Mechanochemical synthesis and crystallization of Li_3BO_3-Li_2CO_3 glass electrolytes. *J. Ceram. Soc. Jpn.* **2016**, *124*, 915−919.
(53) Park, K.; Yu, B. C.; Jung, J. W.; Li, Y. T.; Zhou, W. D.; Gao, H. C.; Son, S.; Goodenough, J. B. Electrochemical Nature of the Cathode Interface for a Solid-State Lithium-Ion Battery: Interface between $LiCoO_2$ and Garnet-$Li_7La_3Zr_2O_{12}$. *Chem. Mater.* **2016**, *28*, 8051−8059.
(54) Han, F.; Yue, J.; Chen, C.; Zhao, N.; Fan, X.; Ma, Z.; Gao, T.; Wang, F.; Guo, X.; Wang, C. Interphase Engineering Enabled All-Ceramic Lithium Battery. *Joule* **2018**, *2*, 497−508.
(55) Schreifels, J. A.; Maybury, P. C.; Swartz, W. E. X-Ray photoelectron spectroscopy of nickel boride catalysts: Correlation of surface states with reaction products in the hydrogenation of acrylonitrile. *J. Catal.* **1980**, *65*, 195−206.
(56) Lin, F.; Markus, I. M.; Doeff, M. M.; Xin, H. L. L. Chemical and Structural Stability of Lithium-Ion Battery Electrode Materials under Electron Beam. *Sci. Rep.* **2015**, *4*, 5694.
(57) Kim, J. W.; Lee, H. G. Thermal and carbothermic decomposition of Na_2CO_3 and Li_2CO_3. *Metall. Mater. Trans. B* **2001**, *32*, 17−24.
(58) Jung, S. H.; Kim, D. H.; Brüner, P.; Lee, H.; Hah, H. J.; Kim, S. K.; Jung, Y. S. Extremely conductive RuO_2-coated $LiNi_{0.5}Mn_{1.5}O_4$ for lithium-ion batteries. *Electrochim. Acta* **2017**, *232*, 236−243.
(59) Kaufmann, E. N.; Brongersma, H. H. *Characterization of Materials*; John Wiley and Sons, Inc.: New York, 2012.
(60) Jung, Y. S.; Cavanagh, A. S.; Riley, L. A.; Kang, S. H.; Dillon, A. C.; Groner, M. D.; George, S. M.; Lee, S. H. Ultrathin Direct Atomic Layer Deposition on Composite Electrodes for Highly Durable and Safe Li-Ion Batteries. *Adv. Mater.* **2010**, *22*, 2172−2176.
(61) Zhu, C.; Usiskin, R. E.; Yu, Y.; Maier, J. The nanoscale circuitry of battery electrodes. *Science* **2017**, *358*, eaao2808.
(62) Gu, W. L.; Hu, L. Y.; Hong, W.; Jia, X. F.; Li, J.; Wang, E. K. Noble-metal-free Co_3S_4-S/G porous hybrids as an efficient electrocatalyst for oxygen reduction reaction. *Chem. Sci.* **2016**, *7*, 4167−4173.
(63) Du, J.; Zhang, T.; Xing, J. L.; Xu, C. L. Hierarchical porous Fe_3O_4/Co_3S_4 nanosheets as an efficient electrocatalyst for the oxygen evolution reaction. *J. Mater. Chem. A* **2017**, *5*, 9210−9216.
(64) Kozen, A. C.; Pearse, A. J.; Lin, C. F.; Noked, M.; Rubloff, G. W. Atomic Layer Deposition of the Solid Electrolyte LiPON. *Chem. Mater.* **2015**, *27*, 5324−5331.
(65) Hakari, T.; Deguchi, M.; Mitsuhara, K.; Ohta, T.; Saito, K.; Orikasa, Y.; Uchimoto, Y.; Kowada, Y.; Hayashi, A.; Tatsumisago, M. Structural and Electronic-State Changes of a Sulfide Solid Electrolyte during the Li Deinsertion-Insertion Processes. *Chem. Mater.* **2017**, *29*, 4768−4774.

DOI: 10.1021/acs.chemmater.8b03321
Chem. Mater. 2018, 30, 8190−8200

(66) Auvergniot, J.; Cassel, A.; Foix, D.; Viallet, V.; Seznec, V.; Dedryvere, R. Redox activity of argyrodite Li_6PS_5Cl electrolyte in all-solid-state Li-ion battery: An XPS study. *Solid State Ionics* **2017**, *300*, 78−85.
(67) Jain, A.; Ong, S. P.; Hautier, G.; Chen, W.; Richards, W. D.; Dacek, S.; Cholia, S.; Gunter, D.; Skinner, D.; Ceder, G.; Persson, K. A. Commentary: The Materials Project: A materials genome approach to accelerating materials innovation. *APL Mater.* **2013**, *1*, 011002.

DOI: 10.1021/acs.chemmater.8b03321
Chem. Mater. 2018, 30, 8190−8200